High-contrast and high-speed multimodal imaging platform: the adaptive optics-confocal rolling slit ophthalmoscope (AO-CRSO)

Léa Krafft, Pierre Senee, Olivier Thouvenin, Daniela Castro-Farias, Michel Paques, Pedro Mecê, Serge Meimon

HIGH CONTRAST AND HIGH SPEED MULTIMODAL IMAGING PLATFORM: THE ADAPTIVE OPTICS - CONFOCAL ROLLING SLIT OPHTHALMOSCOPE (AO-CRSO)

Lea Krafft[1,2], Pierre Senee[1,2,3], Olivier Thouvenin[4], Daniela Castro Farias[2,5], Michel Paques[2,5], Pedro Mecê[2,4,+], and Serge Meimon[1,2,+,*]

[1]DOTA, ONERA, Université Paris Saclay F-91123 Palaiseau, France
[2]Paris Eye Imaging Group, Centre d'Investigation Clinique 1423, Quinze-Vingts National Ophthalmology Hospital, DGOS, INSERM, Paris, France
[3]Quantel Medical, Cournon d'Auvergne, France
[4]Institut Langevin, ESPCI Paris, CNRS, PSL University, Paris, France
[5]Quinze-Vingts Hospital, Paris, France
[+]These authors equally contributed to this work

ABSTRACT

Adaptive optics imaging techniques are invaluable for cellular-level retina visualization. While AO Flood illumination ophthalmoscopes provide distortion-free, high-speed images, they lack contrast. On the other hand, AO scanning laser ophthalmoscopes offer highly contrasted images due to point by point illumination and spatial filtering but suffer from low pixel throughput and distortion artifacts. Our recent advancements, using a DMD integrated AO-FIO, show that we can illuminate and capture multiple spatially separated zones, achieving contrast close to the one of a confocal microscope. Our theoretical framework emphasizes that each zone must be smaller than 100 μm in both directions or smaller than 10 μm in only one direction to minimize the diffuse light component. Building upon these results, we developed a cutting-edge confocal rolling slit ophthalmoscope, able to achieve brightfield contrast similar to a confocal ophthalmoscope, along with phase contrast images. We utilize a classical sCMOS camera with a rolling shutter synchronized with the line source scanning of the field of view. The system makes use of all the incident photons that can be collected, whether singly, multiply scattered or absorbed. Easy digital switching between the darkfield and brightfield, as well as modification of the size and offset of the detection aperture, enhances the adaptability and versatility of this multimodal imaging system, allowing for fine-tuning of imaging modalities and comprehensive exploration of the retina.

Keywords: Retinal imaging, scattering, microscopy, phase contrast, adaptive optics

1. INTRODUCTION

Adaptive optics breakthrough has allowed to reach the diffraction limited resolution and to observe the retinal cells, in-vivo. Achieving detailed visualization of retinal features poses yet a challenge due to the optical complexity of the retina, which is a multilayered organ, situated above the highly scattering choroidal and scleral layers. Multiple scattering that drowns the structures in a diffuse background, making them scarcely noticeable has indeed been a significant hurdle. This challenge prompted a transition from full-field illumination and camera-based detection, as seen in adaptive optics flood illumination ophthalmoscopes (AO-FIO), to the point-by-point scanning approach employed by adaptive optics confocal scanning laser ophthalmoscopes (AO-SLO). The spatial filtering performed by its detection aperture that physically blocks the multiply scattered photons

Further author information: (Send correspondence to S.M.)
S.M.: E-mail: serge.meimon@onera.fr, Telephone: +33 1 46 73 47 83
L.K.: E-mail: lea.krafft@onera.fr, Telephone: +33 1 46 73 47 86

Ophthalmic Technologies XXXIV, edited by Daniel X. Hammer, Kostadinka Bizheva, Georg Schuele, Proc. of SPIE Vol. 12824, 1282404 · © 2024 SPIE
1605-7422 · doi: 10.1117/12.3001609

has demonstrated its ability to provide highly contrasted retinal images of the most reflective structures. However, the previously mentioned techniques lack the capability to visualize the weakly scattering retinal features such as vessel walls or capillaries. The signal from neighbouring highly reflective structures indeed eclipses the latter. In order to circumvent this issue and observe these otherwise imperceptible objects, AO-SLO devices have incorporated an offset aperture configuration. Unlike conventional AO-SLO and AO-FIO, which utilize reflectance contrast by collecting singly backscattered light from the illuminated regions in brightfield mode, the offset aperture AO-SLO technique diverges by employing multiply scattered light. This approach provides contrast originating from phase gradients in a complementary darkfield imaging mode, inspired by oblique back-illumination microscopy.[1–3] Usually performed by adding an offset between the focused illumination beam and the detection aperture, this offset aperture AO-SLO successfully demonstrated high contrast visualization of translucent cells, such as vessel walls, mural cells, photoreceptor inner segments, ganglion cells.[2,4–7]

Despite the complementary brightfield and darkfield imaging modes, the spatial filtering capability provided by AO-SLO detection aperture, comes with a trade-off. As this method involves a point-by-point imaging approach, 2D scanning is required for comprehensive reconstruction of the field of view. The mechanical scanners implemented in AO-SLO present speed limitations compared to fixational eye movements. Consequently, the resulting images are susceptible to distortion artifacts. Limiting the reconstructed field of view is a common trade-off to increase the pixel rate and thus mitigate motion-induced artifacts. For instance, acquisition rates higher than $120Hz$ can be achieved on cropped fields.[8]

Higher pixel throughput can also be achieved by sacrificing confocality in one direction by using a line instead of a point to illuminate the retina with a Line Scanning Laser Ophthalmoscope (LSLO).[9–11] Then, the illumination is scanned over one dimension and the back scattered light is commonly detected with a line camera that spatially filters out the multiply scattered noise. The LSLO first introduced by Hammer et al.[9] could reach a frame rate of $30Hz$. Despite a notable increase in imaging speed, further enhancements are necessary to prevent the impact of eye motion on acquired images. With reported eye movement frequencies reaching up to $100Hz$,[12,13] the Nyquist theorem suggests a minimum imaging rate of $200Hz$ to avoid motion artifacts. Lu et al. achieved retinal imaging at $200Hz$ within a 1.2 deg by 1.2 deg field of view using a high-speed LSLO.[10] Notably, increasing the imaging frame rate by constraining the field of view has shown effectiveness for imaging blood flow in capillaries, as illustrated by Gu et al.[11] They successfully conducted retinal imaging at a rate of $800Hz$ within a field of view measuring 1.2 deg by 0.3 deg using a high-speed LSLO.

Yet, ensuring both high imaging rate and wide field of view is necessary for detecting subtle changes or abnormalities across a larger area as well as for studying blood flow and thus contributing to effective diagnostics and monitoring.

For this reason, developing an AO-FIO with spatial filtering to allow both high contrast brightfield imaging and phase contrast capabilities as opposed to AO-SLO, would definitely be a valuable contribution in retinal imaging. This approach has been initiated by using a digital micro-mirror device (DMD) for partially illuminating the retina with projected patterns and digitally filtering out the detected signal with masks.[14–16] Although this technique serves as a valuable pathfinding tool, the effective frame rate for generating full-field high-contrast images is restricted. In Krafft et al., we reported an effective frame rate up to $25Hz$.[16] This limitation arises because the technique requires multiple image acquisitions to reconstruct the field of view. Additionally, spatial filtering is applied in post-processing to each image of the sequence. Moreover, the process of shaping the illumination in reflection, as executed by the DMD, involves notable power loss.

In this work, we tackle these limitations to demonstrate how an adaptive optics camera-based ophthalmoscope is capable of multimodal, high-speed retinal imaging. We opted for a line illumination, shaped in transmission by line-generating lens for optimal power illumination. High throughput imaging was achieved by synchronizing the scanning of the line with the exposed arrays of pixels of a sCMOS camera, operating in the rolling shutter mode. The rolling shutter enables spatial filtering of the backscattered signal at the acquisition rate, resulting either reflectance contrast similar to that of an AO-SLO in brighfield mode, or phase-contrast images, in darkfield mode. The resulting setup, named the adaptive optics confocal rolling slit ophthalmoscope (AO-CRSO), demonstrates remarkable detection flexibility. It allows for real-time digital switching between darkfield and brightfield modes and provides precise control over the temporal offset between the line and the exposed pixels, as well as pixel exposure time. These capabilities are particularly valuable for enhancing phase contrast.

2. METHOD

2.1 General description of the method

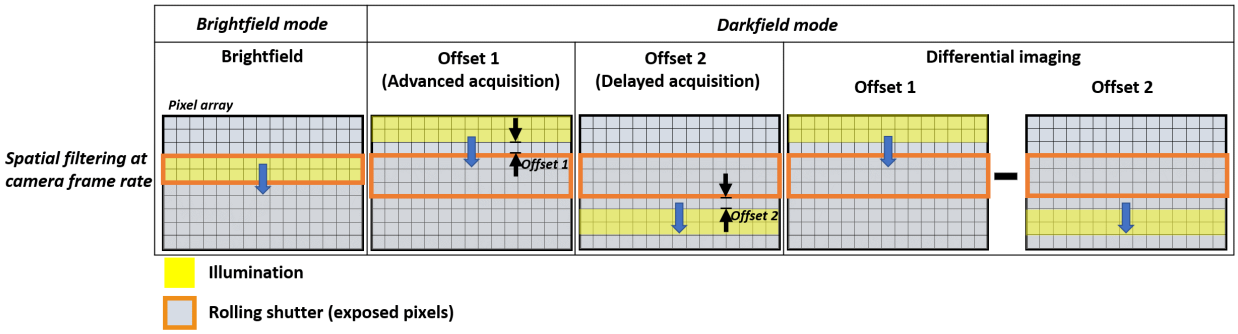

Figure 1. Schematic description of multimodal imaging with the CRSO. Both brightfield and darkfield modes can be generated by adjusting the aperture size of the rolling shutter and its offset relatively to the line illumination.

Figure 2 illustrates the acquisition modes enabled by the CRSO for achieving the multiple contrasts. It relies on a fine monitoring of the detection aperture size and offset relative to the illuminated region during the scan. In practice, the detection aperture corresponds to the electronic rolling shutter of the camera. In brightfield mode, effective spatial filtering of multiply scattered light and out-of-focus light is accomplished by overlapping the center of the backscattered line with the rows of camera pixels which are being exposed. In order to maximize the signal to noise ratio, the size of the detection aperture is chosen to match the size of the line illumination. In darkfield mode, which includes offset 1, offset 2 and differential imaging, the offset is fine-tuned to ensure that the light collected by the pixel rows being exposed comes from non-illuminated regions. Both aperture size of the rolling shutter and offset between the line illumination and the rolling shutter are meticulously adjusted to maximize the contrast of the structures of interest.
The imaging mode as well as the detection parameters are monitored through a customized graphical user interface (GUI) developed in Matlab. The GUI incorporates features to facilitate the configuration of optimal detection parameters and acquisition methods for maximizing contrast. It allows manual adjustment of the offset and aperture size while simultaneously visualizing the contrast of structures on the camera display in real-time. Moreover, it allows to systematically change the delay between illumination and the detection aperture at regular intervals. For high-speed differential imaging, consecutive images are acquired with alternating delays, corresponding to one offset followed by its opposite. Lastly, incorporating brighfield acquisition into this sequence enables to get reflectance and phase contrast information within a single acquisition. Further details on the synchronization can be found in the section 2.3.

2.2 Optical setup

Figure 2-a describes the experimental setup of the system. The AO-FIO platform located at the Paris Quinze-Vingts National Ophthalmology Hospital has been described in previous work.[14,16,17] It was adapted to integrate the CRSO module. The latter benefits from the adaptive optics subsystem to operate as a standalone imaging module of the AO-FIO plateform. Briefly, the illumination systems consists of a fibered broadband Superluminescent Diode (SLD) that emits at 850 nm with a spectral bandwidth of 55 nm and an output power of 20 mW ($SLD850S - A20W$, Thorlabs). The low temporal coherence length of the light source helps mitigating speckles[18] that can originate from interferences between the scattered wavefronts in a disordered medium. The SLD output fiber is directly connected to a collimator. The resulting $0,60mm$ diameter collimated beam is then faned out in one dimension to generate a line source using a Powell lens with a fan angle of 30 deg (♯43 − 473, Edmund Optics).[19] Instead of the non uniform Gaussian laser beam that would be produced by cylindrical lenses, Powell lenses provide an homogeneous illumination distribution in the direction of the line, as shown in its intensity profile along the line, in Fig. 3-c. Its use yet requires to limit the illumination field in the direction of the line in order to minimize power loss. For this reason, the beam is refocused in that direction with an

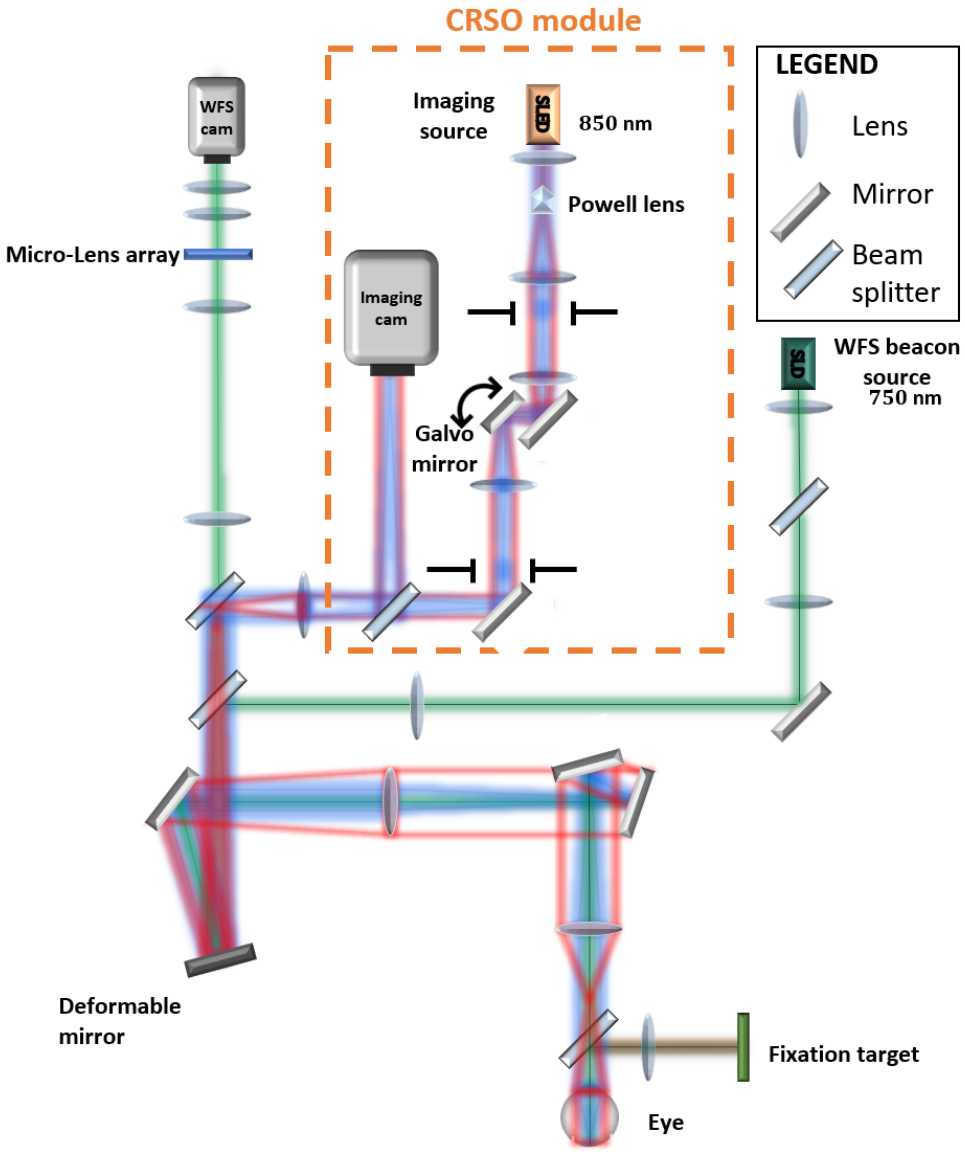

Figure 2. Schematic drawing of the CRSO module (orange rectangle). The length of the line is modelled in red, while its width is depicted in blue. The setup is integrated to the Paris Eye Group AO-FIO plateform, with its adaptive optics module represented in green.

achromatic doublet with a short focal lens. The focal planes of both the Powell and the following doublet were superposed so that the object line is formed on the image focal plane of the lens. The image of the line on the retina is shown in Figure 3-a. Its length covers 4 deg lateral field of view ($1.2mm$ on the retina) of the imaging system. In designing the system, careful consideration was given to set the appropriate thickness of the line illumination to minimize multiple scattering for spatially filtered brightfield images. Guided by theoretical studies[20] and supported by experimental work,[14] the thickness has been set at $10\mu m$ ($7\mu m$ FWHM).
To scan the line across the retina, an achromatic doublet is used to relay the light beam to a galvanometer mirror ($6210H$, Cambridge technology). The galvanometer mirror is optically conjugated with the pupil of the eye. This ensures that the light beam remains stationary at the pupil plane and scans across the retinal plane.

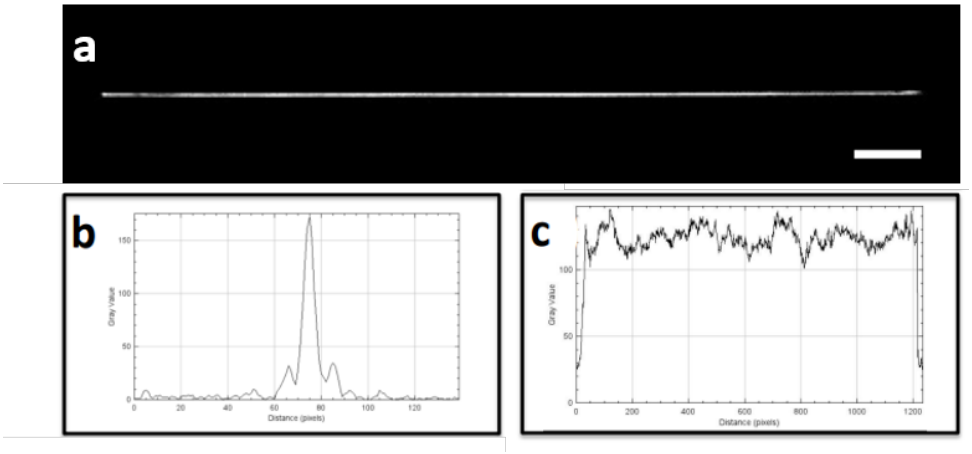

Figure 3. Image (a) and intensity profile of the line illumination on the retina, along its length (b) and its width (c). The width of the line is estimated at $7\mu m$ (FWHM) and its length $1200\mu m$. Scalebar: $100\mu m$.

Additionally, the galvanometer mirror is conjugated with the deformable mirror.
The illumination beam is relayed to the deformable mirror through a telescope setup composed of the two achromatic lenses. The line is focused on the DM along the direction of its length, while the its thickness remains collimated. The incident power is thus distributed over an elongated spot towards the vertical direction. The incoming flux and the size of the beam on the cornea and the retina is be measured to ensure ocular safety, according to the standards. Light is then delivered to the eye by additional relay optics. A beamsplitter located between the two achromatic lenses of the telescope transmits fifty percent of the light power through the rest of the optical system to the deformable mirror before reaching the eye. The backscattered light from the retina propagates in the reverse direction along the incoming path until it reaches the beamsplitter. Half of the incident light is reflected and directed onto the imaging camera (ORCA-Fusion Digital CMOS Camera, Hamamatsu). The camera is monitored with Holovibes software.[21]
The amplitude of the scan can be adjusted to achieve a specified vertical field of view. The scanning speed of the galvanometer mirror is suitable for capturing full-field images over the maximum field of view of 5 deg (approximately 2000 by 2000 pixels) at a rate of $100Hz$ and over half of the field of view (2000 by 1000 pixels) at $200Hz$. The results presented in this work were obtained at $200Hz$ with a scan amplitude covering roughly half of the total field of view.
The imaging camera is equipped with 2304 by 2304 pixels, with a pixel pitch of $6.5\mu m$. It is operated in rolling shutter mode to synchronize the electronic shutter of the camera with the scanning of the galvanometer mirror when acquiring AO-CRSO images. The camera achieves an imaging rate of 200 frames per second (fps) for a region of interest measuring 2048 by 1000 pixels.

2.3 Synchronisation

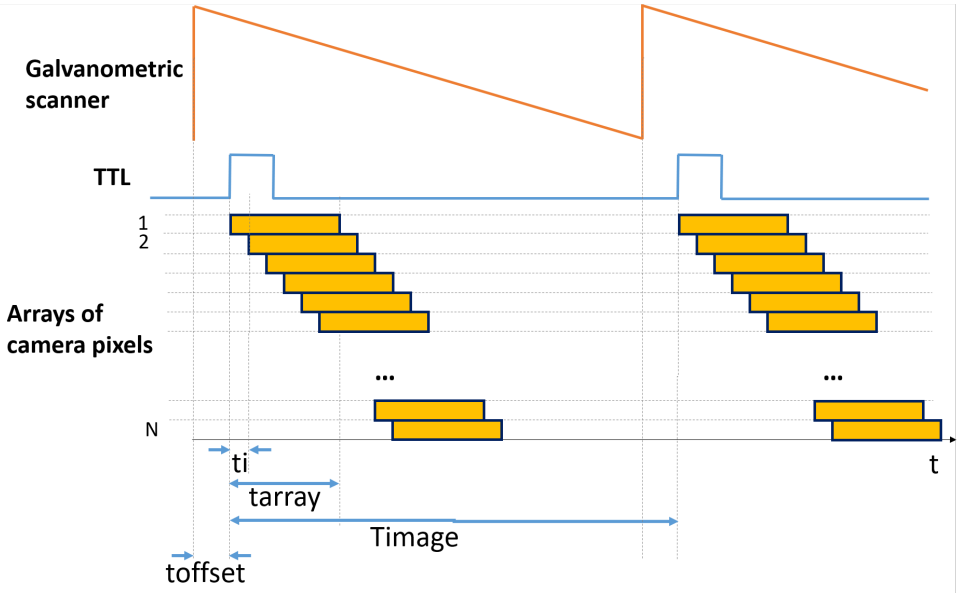

Figure 4. Chronogram of the synchronization between the galvanometer mirror and the sCMOS camera. ti corresponds to the time between the exposure of two consecutive arrays of pixels. $tarray$ is the exposure time of a pixel array. $Timage$ is the period of the TTL signal, namely the time between the start of two consecutive frames. $Toffset$ corresponds to the delay between the scan of the galvanometric mirror and the array of pixels being exposed. The latter is thus set to $0\mu s$ for brightfield acquisitions.

The synchronization between the rolling shutter of the imaging camera and the galvanometric scanner is achieved by transmitting an electronic transistor-transistor logic signal (TTL) to the camera, simultaneously with the application of an analog sawtooth signal to the galvanometer mirror conditioned by the National Instrument DAQ-mx card. The synchronization chronogram is depicted in Figure 4. The TTL signal generated by the computer and sent to the camera thanks to a National Instrument DAQ card.The analog sawtooth signal is generated using a custom-made Matlab code. The trigger signal sent to the camera defines the starting time of the acquisition of a frame. The camera is configured in the "Edge trigger" sub-mode of the External trigger mode. This ensures that the acquisition of a new frame initiates on the rise of the TTL signal. Consequently, the TTL signal defines the frame rate of the imaging sequence. A frame grabber, Active Silicon Frame Grabber (FireBird BASEBOARD 2xCXP662) allows to transfer the images to the system memory.
As depicted in Fig.4, each pixel array is exposed during tarray. At a defined time, as multiple arrays are exposed one can define the width of the camera rolling shutter as the number of pixel arrays exposed. The variable ti represents the time between the exposure of two consecutive arrays. Therefore, it also indicate the period during which the rolling shutter shifts down with a one-array step or its speed per pixel array. Drawing this parallel between temporal considerations of synchronization and an equivalent spatial detection aperture, one can observe the similarity between the offset aperture approach of AO-SLO and the AO-CRSO. Additionally, the variable toffset, representing the delay between the scan of the galvanometric mirror and the exposure of the pixel array, is equivalent to a spatial shift of the detection aperture relative to the line illumination. We consider acquisitions of frames of 1000 arrays of pixels at a rate of $200Hz$, corresponding to $5ms$ exposure time per frame. In order to scan the entire field of view, the speed of the galvanometric mirror is $5\mu s$ per line.
In brightfield images, to maximize the signal-to-noise ratio, it is crucial to maintain the exposure of each pixel array while the scanning line aligns with the array of pixels. Given that the thickness of the line illumination corresponds to 10 pixel arrays, it also aligns with the width of the rolling shutter, resulting in an exposure time of $50\mu s$ per pixel array.
For darkfield images, both the exposure time and the temporal offset (delay or advance) are set within a range

from typically $50\mu s$ to $400\mu s$. In other words, both the aperture size of the rolling shutter and the offset between the line illumination and the expose pixels are set from $7\mu m$ to $59\mu m$.

2.4 Processing

Images of both photoreceptor layer and nerve fiber layer were acquired with the AO-CRSO module at different eccentricities. To compensate for ocular motion, the image stacks went under a registration process before being averaged. This involved adapting to full-field AO-CRSO images a custom-made high-spatial frequency-based phase correlation algorithm, implemented in Matlab and detailed in.[22] Image processing first consists in discarding the blurred frames and those affected by eye blinking. Subsequently, a reference frame is selected from the stack, and the vertical and horizontal shifts resulting from ocular movements are estimated by computing phase correlation maps between each frame and the chosen reference frame. The images presented in the following section were averaged across a stack comprising several hundreds of registered images. For figure 5, AO-SLO images, corresponding to acquisitions of the same region were also performed with the multimodal AO retinal imager (MAORI) (Physical Sciences, Inc., Andover, MA, USA) at the Quinze Vingts Hospital in Paris, described in.[23]

2.5 Image acquisition

In-vivo retinal images were captured from a single healthy young participant.The participant followed institutional guidelines and adhered to the tenets of the declaration of Helsinki. After an explanation of the study's nature and potential outcomes, the subject provided informed consent.
The participant underwent pupil dilation with a 1% tropicamide solution (Mydriaticum, tropicamide 0.5%). Seated in front of the AO-full-field ophthalmoscope and securely stabilized using a chin and forehead rest, the participant was fixating on a yellow crosshair. This target served only to guide the subject's gaze, facilitating exploration of the retina.
The powers of the AO beacon source was $3.7\mu W$ and the imaging source was $0.9mW$. The irradiance of the illumination remained lower than the maximum permissible radiant exposure set by ISO standards (ISO 15004-2 (2007)) for devices classified under group 2.

3. RESULTS

3.1 Brightfield comparison with conventional AO-FIO and AO-SLO

The distinctive attribute of the CRSO lies in its ability to effectively reject multiply scattered photons. To evaluate its spatial filtering capabilities, we conducted a comparative analysis between brightfield CRSO images and those obtained using AO-FIO and confocal AO-SLO, on the same region of the subject.
For a meticulous comparison, we opted to use the same CRSO imaging path for acquiring both AO-FIO and brightfield AO-CRSO images. For AO-FIO images, all the camera pixels were exposed from the start of the acquisition until the exposure time of a single frame of $5ms$. The raw AO-FIO and AO-CRSO images then underwent the same processing algorithm as detailed above. Similar illumination between these images highlights the effect of the rolling shutter on the imaging contrast. The raw AO-FIO, AO-CRSO and AO-SLO images were averaged in order to get similar light irradiance.

	AO-FIO	AO-CRSO	AO-SLO
Michelson contrast	0,17	0,72	0,86
Photoreceptor SNR	5	35	45

Table 1. Comparative measurements of the Michelson contrast and photoreceptor signal-to-noise ratio, conducted among AO-FIO, AO-CRSO, and AO-SLO. These measurements were performed on the data presented in Fig. 5.

Figure 5 shows this comparison in the photoreceptor layer, on a region close to the fovea. 4 deg by 2.4 deg AO-FIO (A) and AO-CRSO (B) images were successfully acquired at $200Hz$. The comparative AO-SLO image (C) was acquired at $30Hz$ over a field of view of 2.2 deg by 1.9 deg. The scattering haze, predominant in the AO-FIO

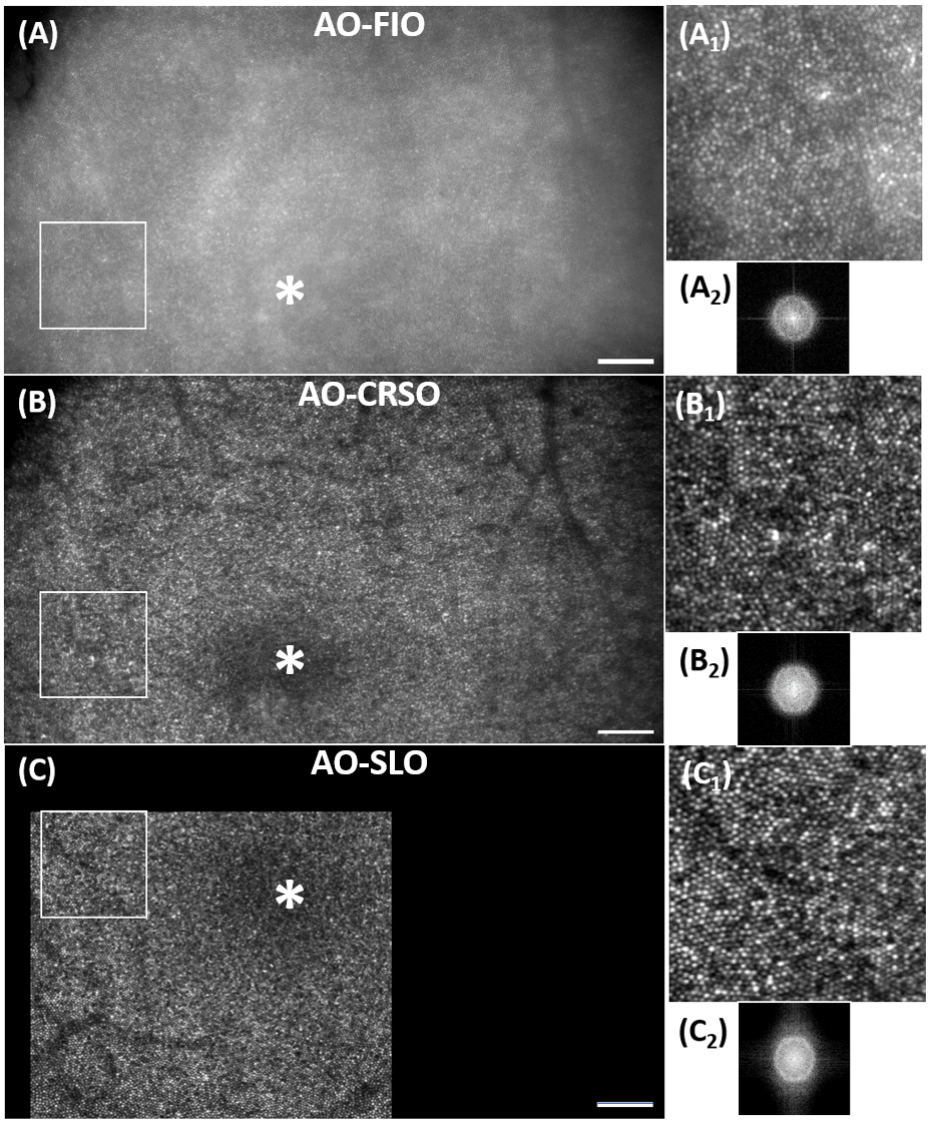

Figure 5. Images of photoreceptor cells near the fovea. 4 deg by 2.4 deg average images acquired with the AO-CRSO with an exposure time of $5ms$ per array (equivalent to global shutter mode) (A), with an exposure time of $50\mu s$ per array (B). 2.2 deg by 1.9 deg confocal AO-SLO image acquired at the same region (C). The white star indicates the center of the fovea. Scale bar: $100\mu m$. Zoom of the same region of 0.6 deg by 0.6 deg (A1, B1 and C1) and their Fourier transform images (A2, B2 and C2). Scale bar: $50\mu m$.

image (A), has been significantly reduced in the AO-CRSO image, making the contrast of the photoreceptors closer to the one in the AO-SLO image (C). This observation is further validated by images (A1, B1, and C1), which represent zoomed-in views of the same retinal region measuring 0.6 deg by 0.6 deg.

The enhancement of contrast is further evident when analyzing the frequency content of the images. The power density spectra depicted in (A2), (B2), and (C2) were obtained by computing the Fourier Transform of (A1), (B1), and (C1). Our specific interest is driven towards how bright the Yellot's ring, which represents the frequency footprint of photoreceptors, gradually increases from the AO-FIO to the AO-SLO

To quantify this improvement, table 1 displays the photoreceptor SNR computed from power density spectra (A2), (B2), and (C2) and the Michelson contrast measured directly on the images (A), (B), and (C). It highlights a 4 fold improvement in Michelson contrast or a 7 fold increase in photoreceptor SNR achieved through the spatial filtering

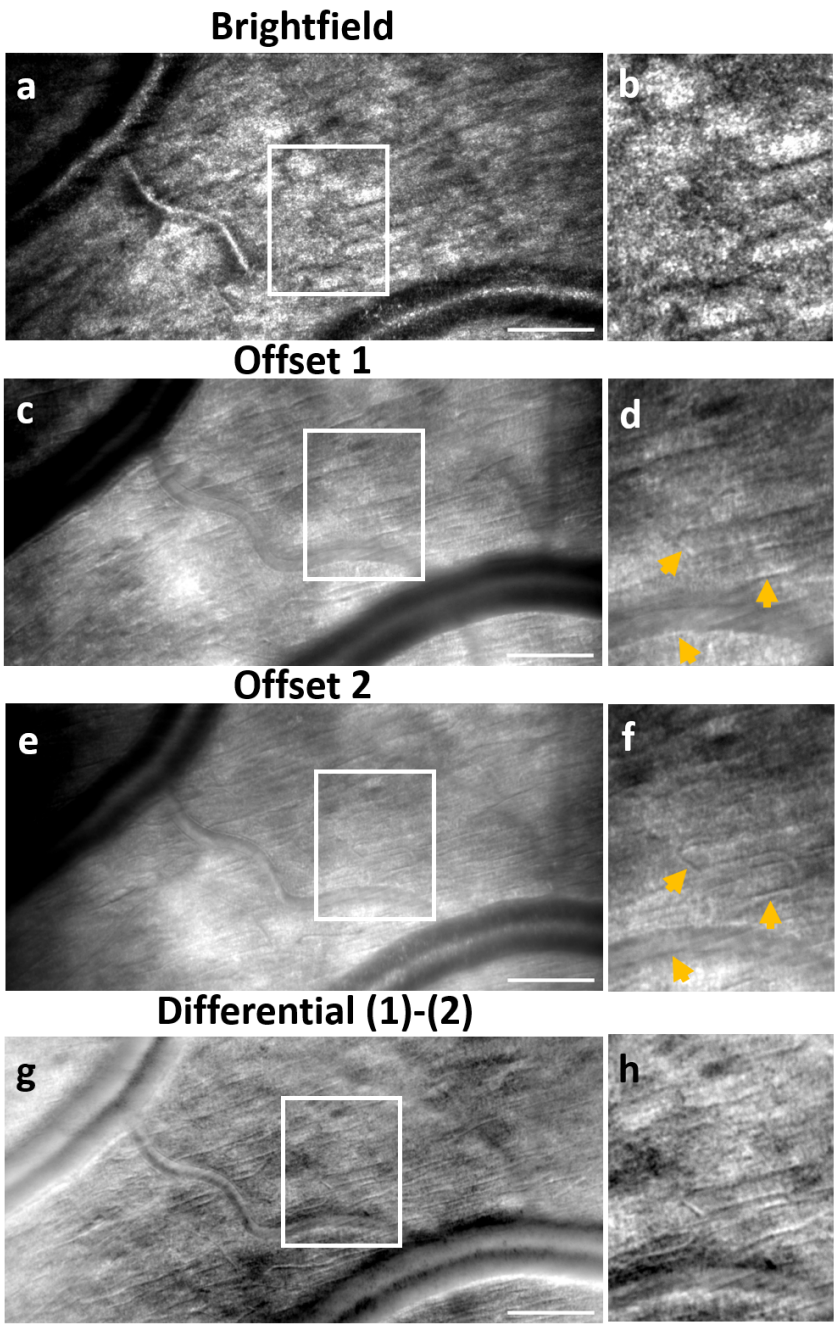

Figure 6. Multimodal imaging with the AO-CRSO reveals images of the nerve fiber layer at the peripheral retina (at 9 temporal degrees). Average images of 4.1 deg by 2.0 deg were acquired with the AO-CRSO in both brightfield (a) and darkfield modes, including offset 1 (c), offset 2 (e), and live differential (g) images. The average live phase contrast images were obtained by sequentially acquiring offset 1 and offset 2 images and subtracting them in real-time. Magnified views of 0.4 deg by 0.5 deg are shown for each acquisition mode (b), (d), (f), (h). In brightfield mode, the exposure time is set to $50\mu s$ per array. In phase contrast mode, the exposure time is adjusted to $300\mu s$ with a delay of $100\mu s$ (approximately $15\mu m$). The yellow arroheads in offset 1 and offset 2 images highlinght the typical inverted contrast between both offsets. Scale bar: $100\mu m$.

of the AO-CRSO (0.72 Michelson contrast and 35 photoreceptor SNR), compared to the AO-FIO (Michelson contrast of 0.17 and photoreceptor SNR of 5). With such enhancements, the AO-CRSO reaches approximately 80% of both the Michelson contrast and photoreceptor SNR of the AO-SLO (0.86 and 45, respectively).

3.2 Multimodal imaging

To advance this proof-of-concept of AO-CRSO towards high-throughput multimodal imaging, we executed imaging sequences that alternated between brightfield and offset 1 and 2 acquisitions, on the nerve fiber layer, at 9 temporal degrees. The resulting images from the same sequence, acquired at $200Hz$ after registration and averaging for each imaging mode (brightfield (a), offset 1 (c), offset 2 (e), and differential (g) images), are presented in Figure 6.

Similar to AO-SLO offset aperture images, the brightfield image (a), (b) favors the strong specular reflection from nerve fibers and the upper external part of blood vessels.[5] By shifting the detection aperture equivalent to $15\mu m$ from the illumination, we effectively filtered out the reflective signal, revealing capillaries, as depicted in (c), (d), (e), and (f).
Magnified views of offset 1 and 2 images (d) and (j) particularly highlight their inverted contrasts, reminiscent of observations in offset aperture AO-SLO,[4,24,25] as indicated by the yellow arrowheads. The vessel contrast is further improved in the differential image (g).
Expanding this study to another retinal eccentricity, Fig. 7 presents two distinct views of the same regions for the photoreceptor layer and the nerve fiber layer.
Effects of spatial filtering clearly visible in the photoreceptor layer. The brightfield mode renders the photoreceptor cells highly contrasted and bright, while the vessels in neighboring layers are optically sectioned and appear dark. The orange arrowheads in Fig. 7-(c) are pointing towards rods. This demonstrates that implementing the CRSO module to the Paris Eye group AO-FIO has not affected the lateral resolution (of $2\mu m$). In phase contrast mode (see Fig 7-(b) and (d)), the differential image reveals the photoreceptor inner segments, akin to the AO-SLO split detection technique.[2] Their precise visualization, whether the outer segment exhibits strong backscattering or not, has proven to be beneficial in the follow-up of gene therapy,[26] blindness, AMD, and glaucoma.[27]
The change in frequency content between the two acquisition modes (a) and (b) can be examined with the power spectral density (PSD) of images (a) and (b) through their Fourier Transform computation. The resulting images (e) and (f) display the frequency footprint of the photoreceptor cells, known as Yellot's ring, in both images.
While the PSD of the brightfield image shows an isotropic distribution of the photoreceptor signal's energy, the PSD of the differential image reveals a preferential energy distribution towards a vertical direction. This direction corresponds to the asymmetric axis, which matches the direction of the offset between the scanning line illumination and the pixel arrays. This observation aligns with multi-offset aperture images, as detailed in Mecê et al.[28]

In the images of the nerve fiber layer, the fiber bed, initially covering the entire field of view in Fig.7-(g), vanishes in Fig.7-(h). This phenomenon resembles the results reported by Chui et al. when utilizing a large aperture with an offset.[4] In the differential image, the capillaries that are hardly visible in the brightfield image, become notably discernible (blue arrowheads).

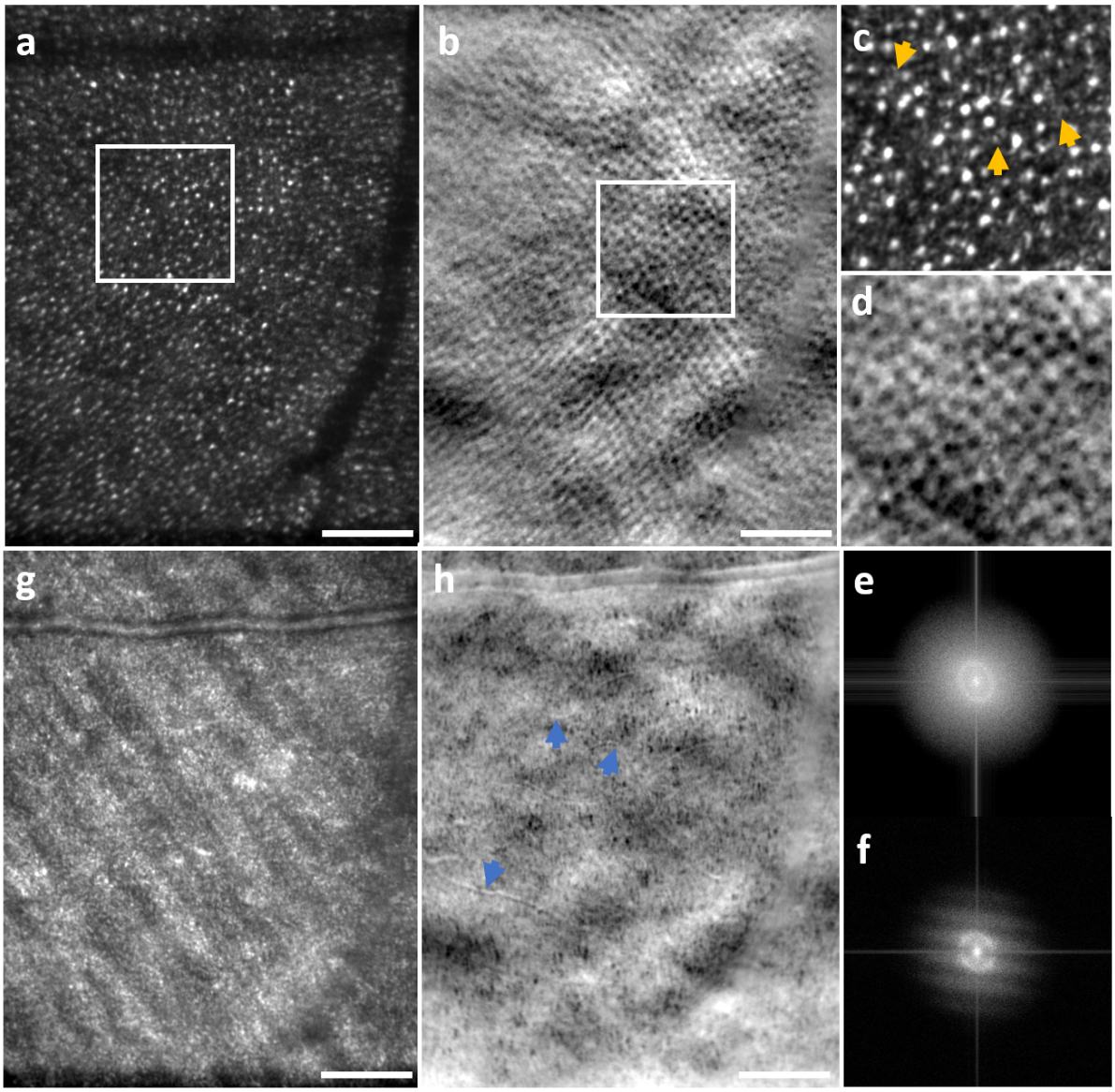

Figure 7. 1.5 deg by 2.0 deg brightfield (a), (g) and differential (b), (h) AO-CRSO images of the same region on both the photoreceptor (a), (b) and the nerve fiber (g), (h) layers, at 9 temporal degrees. 1.0 deg by 1.0 deg magnified views of photoreceptors are shown in brightfield (c) and differential imaging (d) modes, as well as the corresponding power density spectra (g) and (h) computed from (a) and (b). The blue arrowheads in the differential image of the nerve fiber layer (h) point towards capillaries. The orange arrowheads in the magnified view of the photoreceptors in brightfield (c) point towards rods. Scale bar: $100\mu m$.

4. DISCUSSION

This study demonstrates the flexibility and efficiency of the AO-CRSO in tailoring the imaging process to specific contrast requirements. To evaluate this capacity even further, we conducted a parametric study to evaluate the contrast evolution when varying the offset between the line illumination while keeping the same exposure time of $300\mu s$ per line (corresponding to an aperture size of $44\mu m$). In Fig. 8, we observe a gradual change in contrast of differential images in the the nerve fiber layer with increasing offsets. Smaller offsets enhance the contrast

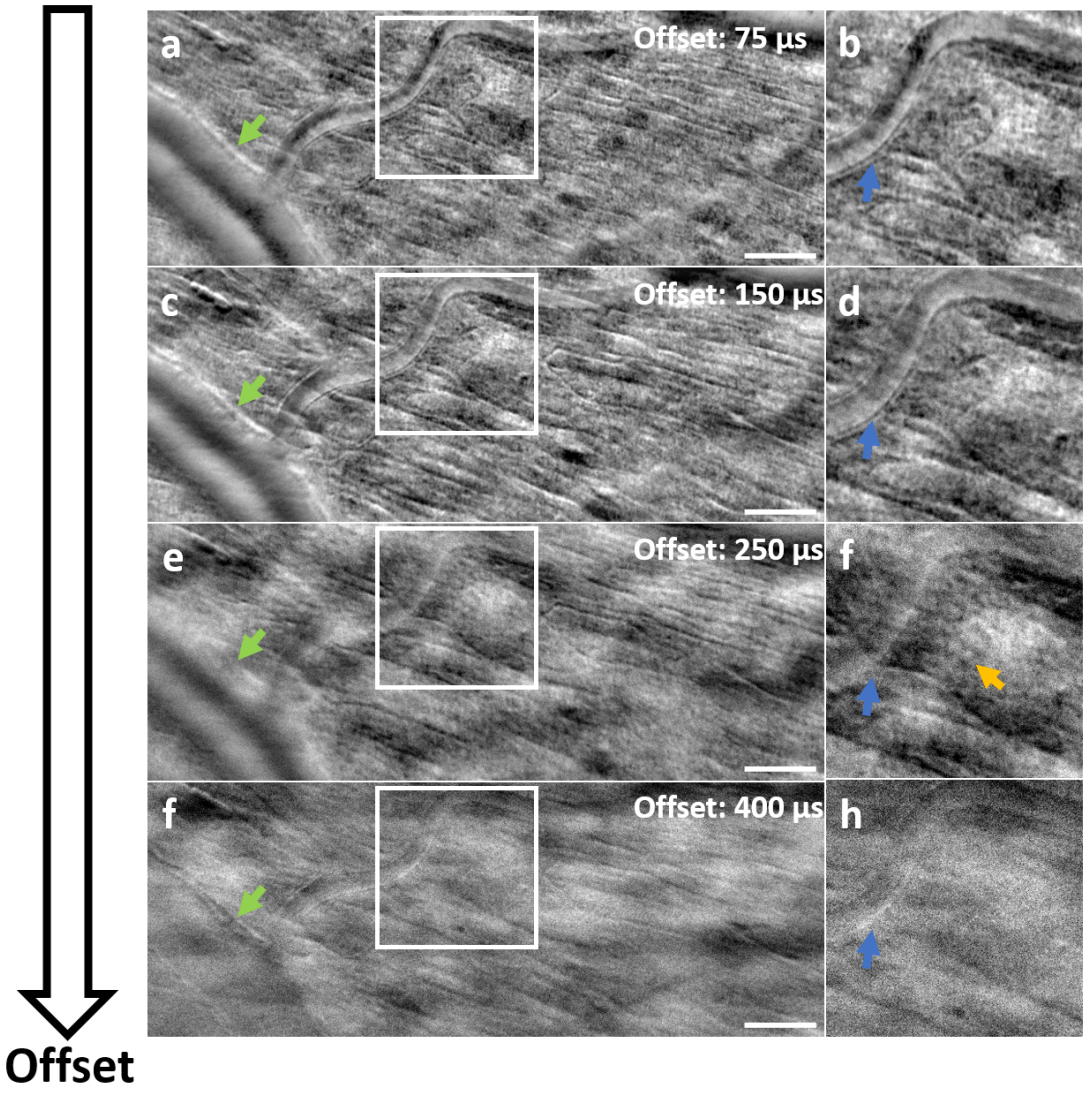

Figure 8. 3.2 deg by 1.2 deg differential images of the nerve fiber layer, as the delay between the illumination and the rolling shutter increases, at a constant exposure time of $300\mu s$. The delays were set at $75\mu s$ (a), $150\mu s$ (b), $250\mu s$ (c), and $400\mu s$ (d). The corresponding offsets are $11\mu m$ (a), $22\mu m$ (b), (c), (d). The green arrowheads highlight the same large vessel for each offset. The blue arrowheads in the magnified views show the same vessel under different offsets. The yellow arrowhead in (f) points towards putative ganglion cells. Scale bar: $100\mu m$.

of capillaries and vessel walls. This contrast begins to dissipate at $250\mu m$ (equivalent to $37\mu m$). The altering appearance of the vessel wall indicated by the blue arrowhead illustrates this trend. Larger features, such as the vessel pointed out by the green arrowhead, remain visible at larger offsets before fading at $400\mu s$ (equivalent to $60\mu m$). Notably, putative ganglion cells (size: 10–$12\mu m$) become visible with a consistent size and in a manner similar to images previously demonstrated in multi-offset AO-SLO,[7] at an offset of $250\mu s$ ($37\mu m$), as indicated by the yellow arrowhead in the magnified view. Achieving high precision in offset settings is crucial to observe these cells, as they become obscured at the subsequent offset of $400\mu s$.

In Fig. 8, we observe a gradual change in contrast as the offset increases. While the smallest offsets favor the contrast of capillaries and vessel walls, their contrast beging to dissipate at $250\mu m$ (equivalent to $37\mu m$). The varying aspect of the vessel wall pointed by the blue arrowhead illustrates this tendency. Bigger features as

the vessel pointed by the green arrowhead are visible at bigger offsets before fading. Particularly interesting, at offset $250\mu s$, ($37\mu m$), displays putative ganglion cells (size: 10–$12\mu m$ as pointed by the yellow arrowhead on the magnified view.

Along with the system's versatility, these results also highlight the ability of the AO-CRSO to perform imaging with spatial filtering similarly to AO-SLO technique but with an asset of being at the camera pixel rate.

This marks a notable evolution from conventional camera-based pattern projection multimodal retinal imaging approaches.[16] Specifically, the AO-CRSO's rolling shutter camera eliminates the need for additional digital filtering in post-processing required with the pattern projection approach. What adds further value for clinical practice is its capability for direct visualization of the retina in the desired mode and synchronization settings during eye examinations.

Additionally, the ability to switch detection modes within a single acquisition, without affecting the frame rate enables the system to perform rapid multimodal imaging. In comparison to offset aperture AO-SLO, the AO-CRSO cannot achieve simultaneous bright and darkfield imaging. However, with the alternating acquisition modes, the delay between consecutive raw brightfield and offset images can be reduced to one frame, that is $5ms$ at $200Hz$. Consequently, complementary data in brightfield and differential imaging modes can be obtained at an effective rate of approximately $67Hz$ for a field of view of 4 deg by 2.4 deg.

More particularly, high throughput phase contrast imaging, represents a valuable asset of the AO-CRSO. Offset aperture acquisitions alternating advanced and delayed detection with the same offset, allows to get direct visualization of the blood flow in the microvasculature. Giving access to a quantitative counting of erythrocytes provides a distinctive benefit for the in-depth examination of vascular disease over time in humans.[11]

Narrowing the field of view to 1 deg by 4 deg, we successfully captured individual red blood cells within capillaries at a rapid imaging rate of $400Hz$. Figure 9 depicts the perfusion map of the area where red blood cell flow was captured, computed from differential images. Reslicing the $400Hz$ video along the selected capillary's direction enabled to create the kymograph in (b). This technique, previously used on brightfield images,[29] allowed us to retrieve blood cell speed within vessels. Using the same method, blood flow in the capillary was estimated from $0.68mm/s$ to $1.35mm/s$, consistent with ranges presented in prior work. Additionally, by reslicing perpendicularly to the same capillary, blood flow was measured by counting individual red blood cells, employing a technique demonstrated in mice.[30–32] The corresponding kymograph in (c) indicates a blood flow of 40 to 100 red blood cells per second, aligning with in vivo measurements in human retinal capillaries presented in.[32]

Adapting the image processing method would help improve the imaging quality over the entire field of view bringing a more accurate estimation of potential biomarkers such as blood flow. In fact, imaging fine dynamic functional processes such as moving red blood cells over the full field and the entire imaging sequence makes the imaging quality even more sensitive to registration performances at subpixel level. Implementing to our processing scheme stripe-based image registration method seem particularly adapted to this challenge.[33,34] In fact, the precision of the registration relies on the reference frame, which must be carefully selected to be with minimum distortion. High-speed imaging enabled by the AO-CRSO may facilitate better and easier generation of a reference frame with minimal intra-frame distortion.

5. CONCLUSION

The AO-CRSO has demonstrated its ability to utilize both directly scattered and multiply scattered photons to image various structures such as fibers, vessels, capillaries, or photoreceptors, employing both brightfield and phase contrast modes. Successful image acquisition has been demonstrated across different regions of both the foveal and peripheral retina.

Proof-of-concept images exhibit a notable contrast enhancement compared to AO-FIO images, approaching the contrast levels of images obtained at lower rates with confocal systems. This enhancement has been achieved while maintaining a resolution sufficient for observing the structures of the smallest cells, such as foveal center cones and rods.

Notably, features observed in offset images closely resemble those seen in phase contrast images acquired with offset aperture AO-SLO, suggesting significant potential for enhancing visibility and broadening the range of structures revealed by this technique.

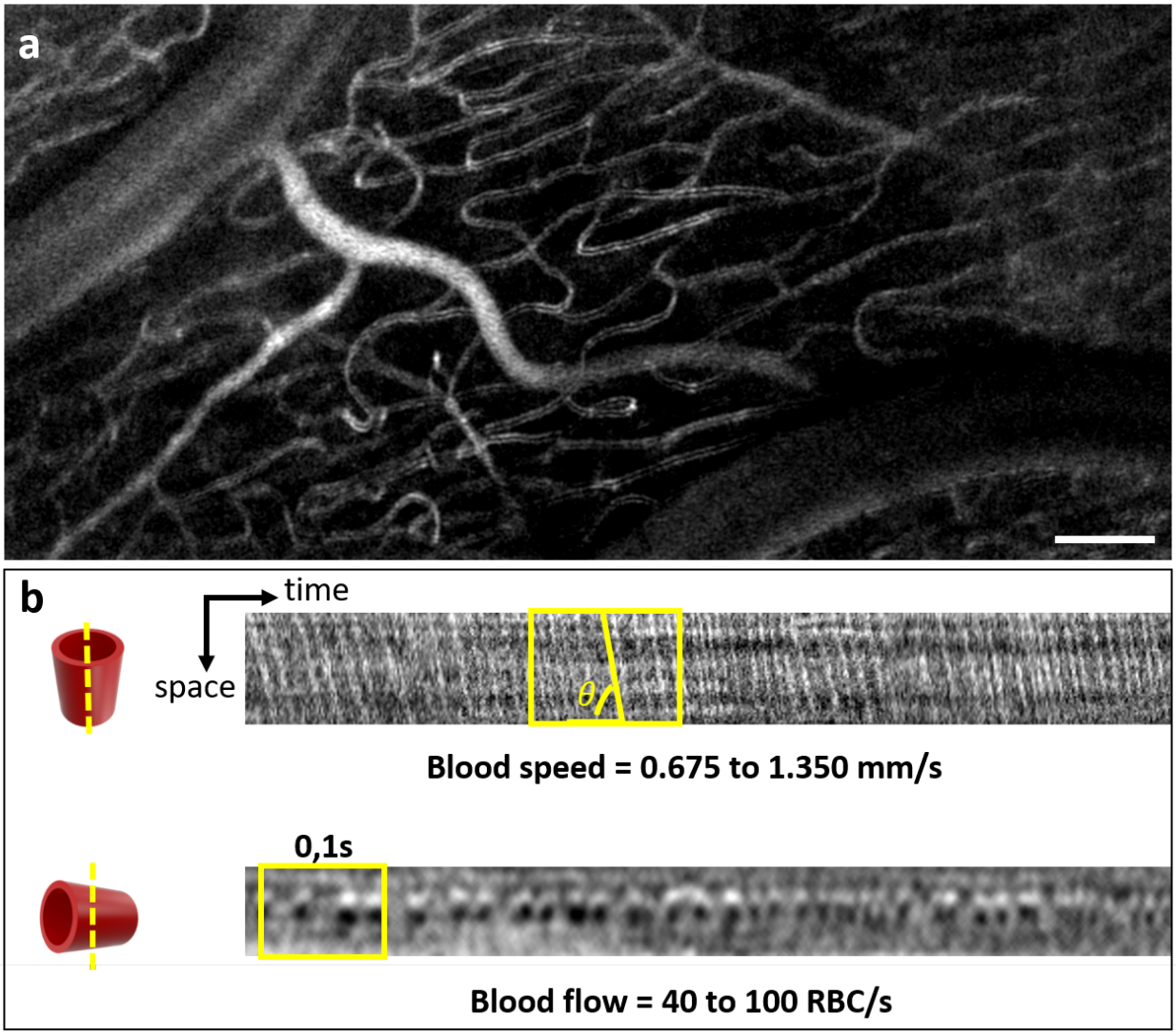

Figure 9. Red blood cell counting is performed on the motion contrast differential image. The 3.9 deg by 1.9 deg motion contrast image (a) is generated from the same image sequence as in Fig. 7-(g). The kymograph of the red blood cell flow is computed by reslicing the capillary section (in yellow) from the $400Hz$ image sequence in the direction of the capillary ((b) first row). Blood flow is measured using a kymograph of the red blood cell flow from the same capillary section through perpendicular reslicing for counting individual red blood cells ((b) second row). Scalebar: $100\mu m$.

Furthermore, the demonstrated flexibility to adjust the detection offset for optimizing imaging contrast on specific structures underscores the versatility of the AO-CRSO. The capability to acquire images using the alternating acquisition modes minimizes intra-frame motion-induced artifacts, opening new perspectives for functional imaging such as blood flow measurements and the study of retinal diseases.

ACKNOWLEDGMENTS

The authors would like to thank Elena Gofas and Kate Grieve for their the fruitful discussions and for providing the AO-SLO dataset. We also want to thank Michael Atlan for his technical support on Holovibes software.

Office National d'études et de Recherches Aérospatiales (PRF TELEMAC); Agence Nationale de la Recherche (ANR-18-IAHU-0001, ANR-22-CE19-0010-01).

REFERENCES

[1] Ford, T. N., Chu, K. K., and Mertz, J., "Phase-gradient microscopy in thick tissue with oblique back-illumination," **9**(12), 1195–1197.

[2] Scoles, D., Sulai, Y. N., Langlo, C. S., Fishman, G. A., Curcio, C. A., Carroll, J., and Dubra, A., "In vivo imaging of human cone photoreceptor inner segments," **55**(7), 4244.

[3] Laforest, T., Künzi, M., Kowalczuk, L., Carpentras, D., Behar-Cohen, F., and Moser, C., "Transscleral optical phase imaging of the human retina," **14**(7), 439–445.

[4] Chui, T. Y. P., VanNasdale, D. A., and Burns, S. A., "The use of forward scatter to improve retinal vascular imaging with an adaptive optics scanning laser ophthalmoscope," **3**(10), 2537.

[5] Chui, T. Y. P., Gast, T. J., and Burns, S. A., "Imaging of vascular wall fine structure in the human retina using adaptive optics scanning laser ophthalmoscopy," **54**(10), 7115.

[6] Sulai, Y. N., Scoles, D., Harvey, Z., and Dubra, A., "Visualization of retinal vascular structure and perfusion with a nonconfocal adaptive optics scanning light ophthalmoscope," **31**(3), 569.

[7] Gofas-Salas, E., Rui, Y., Mecê, P., Zhang, M., Snyder, V. C., Vienola, K. V., Lee, D. M. W., Sahel, J.-A., Grieve, K., and Rossi, E. A., "Design of a radial multi-offset detection pattern for in vivo phase contrast imaging of the inner retina in humans," **13**(1), 117.

[8] Burns, S. A., Elsner, A. E., Sapoznik, K. A., Warner, R. L., and Gast, T. J., "Adaptive optics imaging of the human retina," **68**, 1–30.

[9] Hammer, D. X., Ferguson, R. D., Ustun, T. E., Bigelow, C. E., Iftimia, N. V., and Webb, R. H., "Line-scanning laser ophthalmoscope," **11**(4), 041126.

[10] Lu, J., Gu, B., Wang, X., and Zhang, Y., "High-speed adaptive optics line scan confocal retinal imaging for human eye," **12**(3), e0169358.

[11] Gu, B., Wang, X., Twa, M. D., Tam, J., Girkin, C. A., and Zhang, Y., "Noninvasive in vivo characterization of erythrocyte motion in human retinal capillaries using high-speed adaptive optics near-confocal imaging," **9**(8), 3653.

[12] Ezenman, M., Hallett, P., and Frecker, R., "Power spectra for ocular drift and tremor," **25**(11), 1635–1640.

[13] Riggs, L. A., Armington, J. C., and Ratliff, F., "Motions of the retinal image during fixation*," **44**(4), 315.

[14] Krafft, L., Gofas-Salas, E., Lai-Tim, Y., Paques, M., Mugnier, L., Thouvenin, O., Mecê, P., and Meimon, S., "Partial-field illumination ophthalmoscope: improving the contrast of a camera-based retinal imager," **60**(31), 9951.

[15] Lee, S., Choi, S. S., Meleppat, R. K., Zawadzki, R. J., and Doble, N., "Programmable, high-speed, adaptive optics partially confocal multi-spot ophthalmoscope using a digital micromirror device," **48**(3), 791–794.

[16] Krafft, L., Senée, P., Gofas, E., Thouvenin, O., Atlan, M., Paques, M., Meimon, S., and Mecê, P., "Multimodal high-resolution retinal imaging using a camera-based DMD-integrated adaptive optics flood-illumination ophthalmoscope," **48**(14), 3785.

[17] Gofas-Salas, E., Mecê, P., Petit, C., Jarosz, J., Mugnier, L. M., Montmerle Bonnefois, A., Grieve, K., Sahel, J., Paques, M., and Meimon, S., "High loop rate adaptive optics flood illumination ophthalmoscope with structured illumination capability," **57**(20), 5635.

[18] Halpaap, D., García-Guerra, C. E., Vilaseca, M., and Masoller, C., "Speckle reduction in double-pass retinal images," **9**(1), 4469.

[19] Powell, I., "Linear deiverging lens."

[20] Krafft, L., "Spatial filtering for flood illumination ophthalmoscope."

[21] "Holovibes."

[22] Mecê, P. B., "4d exploration of the retina for adaptive optics-assisted laser photocoagulation."

[23] Hammer, D. X., Daniel Ferguson, R., Mujat, M., Patel, A., Plumb, E., Iftimia, N., Chui, T. Y. P., Akula, J. D., and Fulton, A. B., "Multimodal adaptive optics retinal imager: design and performance," **29**(12), 2598.

[24] Rossi, E. A., Granger, C. E., Sharma, R., Yang, Q., Saito, K., Schwarz, C., Walters, S., Nozato, K., Zhang, J., Kawakami, T., Fischer, W., Latchney, L. R., Hunter, J. J., Chung, M. M., and Williams, D. R., "Imaging individual neurons in the retinal ganglion cell layer of the living eye," **114**(3), 586–591.

[25] Guevara-Torres, A., Williams, D. R., and Schallek, J. B., "Origin of cell contrast in offset aperture adaptive optics ophthalmoscopy," **45**(4), 840.

[26] Pang, J.-j., Deng, W.-T., Dai, X., Lei, B., Everhart, D., Umino, Y., Li, J., Zhang, K., Mao, S., Boye, S. L., Liu, L., Chiodo, V. A., Liu, X., Shi, W., Tao, Y., Chang, B., and Hauswirth, W. W., "AAV-mediated cone rescue in a naturally occurring mouse model of CNGA3-achromatopsia," **7**(4), e35250.

[27] Jackson, G. R., Owsley, C., and Curcio, C. A., "Photoreceptor degeneration and dysfunction in aging and age-related maculopathy," **1**(3), 381–396.

[28] Mecê, P., Gofas, E., Rui, Y., Zhang, M., Sahel, J.-A., and Rossi, E. A., "Spatial frequency-based image reconstruction to improve image contrast in multi-offset adaptive optics ophthalmoscopy."

[29] Joseph, A., Guevara-Torres, A., and Schallek, J., "Imaging single-cell blood flow in the smallest to largest vessels in the living retina," **8**, e45077.

[30] Guevara-Torres, A., Joseph, A., and Schallek, J. B., "Label free measurement of retinal blood cell flux, velocity, hematocrit and capillary width in the living mouse eye," **7**(10), 4228.

[31] Dholakia, K. Y., Guevara-Torres, A., Feng, G., Power, D., and Schallek, J., "In vivo capillary structure and blood cell flux in the normal and diabetic mouse eye," **63**(2), 18.

[32] Gu, B., Sarraf, D., Ip, M., Sadda, S. R., and Zhang, Y., "In vivo measurement of the lineal density of red blood cells in human retinal capillaries using high speed adaptive optics ophthalmoscopy," **46**(14), 3392–3395.

[33] Vogel, C. R., Arathorn, D. W., Roorda, A., and Parker, A., "Retinal motion estimation in adaptive optics scanning laser ophthalmoscopy," **14**(2), 487–497.

[34] Zhang, M., Gofas-Salas, E., Leonard, B. T., Rui, Y., Snyder, V. C., Reecher, H. M., Mecê, P., and Rossi, E. A., "Strip-based digital image registration for distortion minimization and robust eye motion measurement from scanned ophthalmic imaging systems," **12**(4), 2353.